CHEMISTRY OF MATERIALS
Cite This: Chem. Mater. 2019, 31, 5509−5518
Article
pubs.acs.org/cm

Vapor Phase Infiltration of Metal Oxides into Nanoporous Polymers for Organic Solvent Separation Membranes

Emily K. McGuinness,[†,§] Fengyi Zhang,[‡,§] Yao Ma,[‡] Ryan P. Lively,*[,‡] and Mark D. Losego*[,†]

[†]School of Materials Science and Engineering, [‡]School of Chemical and Biomolecular Engineering, Georgia Institute of Technology, Atlanta, Georgia 30332, United States

Supporting Information

ABSTRACT: Membrane-based organic solvent separations promise a low-energy alternative to traditional thermal separations but require materials that operate reliably in chemically aggressive environments. While inorganic membranes can withstand demanding conditions, they are costly and difficult to scale. Polymeric membranes, such as polymer of intrinsic microporosity 1 (PIM-1), are easily manufactured into forms consistent with large-scale separations (e.g., hollow fibers) but perform poorly in aggressive solvents. Here, a new postfabrication membrane modification technique, vapor phase infiltration (VPI), is reported that infuses PIM-1 with inorganic constituents to improve stability while maintaining the polymer's macroscale form and nanoporous internal structure. The atomic-scale metal oxide networks within these hybrid membranes protect PIM-1 from swelling or dissolving in solvents. This stability translates to improved separation performance in a variety of solvents, including solvents capable of dissolving PIM-1. The infiltrated inorganic phase also appears to give new control over solute sorption in organic solvent nanofiltration (OSN). These hybrid membranes further show promising performance for organic solvent reverse osmosis (OSRO) separations in challenging solvents, even at small-molecular-weight differentials (14 Da). Because the VPI process can be integrated with state-of-the-art membrane modules, this treatment could be readily adopted into the large-scale manufacturing of advanced membranes.

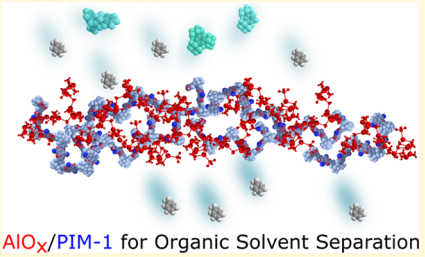

INTRODUCTION

Modern chemical manufacturing depends on efficient chemical separations. Today, most separations are achieved with energy-intensive thermal approaches based on phase changes (e.g., distillation), which account for 10−15% of global energy usage.[1] In contrast, membrane separations, which differentiate molecules based on variations in molecular size, shape, and physicochemical interaction parameters, require minimal energy input. For instance, membrane-based desalination uses 90% less energy than the most optimized thermally driven processes (i.e., highly engineered multistage flash evaporation consumes approximately 45 kWh/m^3, whereas commercial reverse osmosis plants consume approximately 4.5 kWh/m^3).[2]

Most current commercial membrane separation technologies are deployed for gaseous chemicals or aqueous media (e.g., brine). However, membrane usage in organic solvent separation (e.g., xylene separation, organic solvent dehydration, product separation of synthesis solution, etc.) is becoming more prevalent in the modern chemical industry due to its potential energy and carbon savings. For instance, the separation of benzene derivatives requires approximately 430 TWh of energy each year;[1] membrane processes such as organic solvent nanofiltration (OSN) and organic solvent reverse osmosis (OSRO) can potentially drive this energy cost down by an order of magnitude.[3] For successful integration into industrial processing, OSN and OSRO processes require membranes that retain their mechanical integrity and microstructure when operating in aggressive organic solvents.[4] State-of-the-art organic solvent separation membrane materials include zeolites,[5,6] metal-organic frameworks,[7] carbon molecular sieves,[3,8] porous organic cages,[9] porous ceramics,[10] cross-linked polymer networks,[11,12] microporous polymers,[13] conjugated microporous polymers,[14] etc. While inorganic membranes, like zeolites, can be stable in organic solvents, they are costly and challenging to scale up in a defect-free manner.[12] Solution-processable polymers can be mass-produced into defect-free membranes but lack the requisite levels of organic solvent stability. The stability of some polymeric membranes can be improved by promoting cross-linking through the careful selection of polymer chemistry and processing.[11,12] However, this method cannot be expanded to all polymer chemistries.

One polymer class of interest for organic solvent separation is polymers of intrinsic microporosity.[11,13] A prototypical polymer of intrinsic microporosity is the polymer of intrinsic microporosity 1 (PIM-1). At ambient conditions, PIM-1 is a solution-processable, rigid, glassy polymer with high levels of microporosity, but like other polymer membranes, it has limited stability and selectivity when exposed to plasticizing solvents or highly sorptive solutes.[8,13,15−17] Several postfabrication techniques have been developed to enhance the solvent

Received: March 21, 2019
Revised: July 3, 2019
Published: July 18, 2019

DOI: 10.1021/acs.chemmater.9b01141
Chem. Mater. 2019, 31, 5509−5518

stability of polymer membranes like PIM-1, including cross-linking to create interconnected polymer networks and thermal pyrolysis to create carbon molecular sieves.[3,8,18] While these techniques show promise toward creating solvent-stable scalable membranes, both lead to dramatic changes in the membrane's microscopic structure and a higher probability of defect formation. These postfabrication techniques also consume large amounts of chemicals and solvents, require additional equipment, and generate added costs.

Vapor phase infiltration (VPI) is a gas-phase, solvent-free process that has emerged from the atomic layer deposition (ALD) community to load the bulk of polymers with inorganics; metal oxides are frequently chosen as the inorganic.[19−23] While atomic layer deposition has been used on polymeric membranes to modify wettability,[24,25] create anticrude oil membranes,[26] provide antifouling properties,[27−29] implement catalyst sites,[30,31] and modify meso-/macropore sizes,[31,32] the ALD process is fundamentally different from VPI. ALD uses short vapor pulses of metal-organic precursors to deposit a coating on freely exposed solid/gas surfaces and typically requires tens to hundreds of cycles to deposit nanometers of material.[33−35] In contrast, VPI uses long precursor exposure times to sorb and diffuse metal-organic precursors into the bulk of a polymer to create an organic−inorganic hybrid material.[19−23] Depending upon precursor and polymer chemistry, a single VPI exposure cycle can be sufficient to achieve inorganic loadings of several weight percentages within the subsurface or bulk of a polymer.[36,37] Previously, VPI has been used to load polysulfone membranes with aluminum oxide,[38] increase the resilience of polymeric nanopillars,[39] strengthen spider silk,[40] and provide UV protection to Kevlar fibers.[41] The VPI kinetics and final hybrid material's physiochemical structure vary with polymer chemistry, polymer microstructure, metal-organic precursor chemistry, and processing temperature.[19−23] With regard to polymer chemistry, VPI behavior ranges from the formation of semibound intermediate states (such as with amine and nitro functional groups),[42] to temperature-dependent covalent bonding (such as with carbonyl functionality), to immediate, irreversible bonding (hydroxyl groups). The interplay between different polymer/metal-organic precursor systems is complex and is still an area of ongoing study.[19−23]

This article is the first known report of using VPI to promote membrane stability in harsh chemical environments. Different from cross-linking or pyrolysis, VPI leaves the polymer microstructure and macroscale form factor largely unchanged.[42−44] A further advantage of VPI is the ease of large-scale application. Whereas cross-linking requires processing with new solvents and chemicals and pyrolysis requires high temperatures (>400 °C), VPI can be accomplished within the standard membrane modules with minimal investment in additional equipment (Figure S1). The mild reaction environment (vacuum levels up to 1 Torr and 90 °C) can be supplied by general roughing vacuum pumps and heating media. While some of the chemicals involved in VPI are pyrophoric, their regular use in the semiconductor industry has led to the evolution of engineering and operational safeguards. In this proof-of-concept study, we demonstrate that VPI can create hybrid polymer/metal oxide membranes that increase chemical stability, retain microporosity, and improve organic solvent nanofiltration performance even in deleterious solvents. Furthermore, VPI-synthesized hybrid membranes are capable of separating solvent systems with incredibly small-molecular-weight differentials, thus expanding the use of these membranes from organic solvent nanofiltration to organic solvent reverse osmosis.

EXPERIMENTAL METHODS

Polymer of Intrinsic Microporosity 1 (PIM-1) Synthesis. A room-temperature condensation of tetrafluoroterephthalonitrile (TFTPN, Alfa Aesar) and 5,5′,6,6′-tetrahydroxy-3,3,3′,3′-tetramethyl-1,1′-spirobisindane (TTSBI, Alfa Aesar) was conducted in anhydrous dimethylformamide (DMF, Alfa Aesar) in the presence of K_2CO_3 (Alfa Aesar) fine powders for 72 h.[8] The reaction was conducted at 65 °C with stirring. Prior to synthesis, TTSBI and TFTPN were purified via vacuum sublimation and recrystallization, respectively.[8] Monomers and oligomers were removed by postsynthesis washing using DMF and methanol. The purified PIM-1 (M_n = 50 200, M_w/M_n = 1.65) was then stored in sealed jars. The molecular weight was determined by gel permeation chromatography in tetrahydrofuran compared with polystyrene standards. Unless declared, all organic solvents used in this paper were generic, ACS grade purchased from Sigma-Aldrich or Alfa Aesar without further treatment. Styrene dimers and polystyrene oligomers were purchased from Agilent. Matrimid 5218 was purchased from Huntsman. *p*-Xylylenediamine was purchased from Sigma-Aldrich.

Flat PIM-1 Membrane Casting. The dry PIM-1 powder was dissolved in anhydrous chloroform with a mass ratio of 1:200. After complete dissolution, the PIM-1 solution was filtered through a PTFE filter with 0.45 μm pores. The clear yellow PIM-1 solution was then transferred into a nitrogen glovebag that had been saturated with chloroform. The PIM-1 solution was then poured into a PTFE Petri dish. After 48 h of slow evaporation, the flat PIM-1 membrane was transferred into a vacuum oven (990 mbar, 80 °C) to dry thoroughly. The thickness of the flat PIM-1 membranes was controlled by varying the amount of PIM-1 solution poured into PTFE Petri dishes. These flat PIM-1 membranes were then used to study VPI infiltration depth profiles, contact angle, and transmission Fourier-transform infrared (FTIR).

PIM-1 Hollow Fiber Membrane Spinning. PIM-1 hollow fiber membranes were fabricated via dry-wet spinning, as described by Jue et al.[45] As a result of phase inversion, PIM-1 hollow fiber membranes exhibit hierarchical porosity, which minimizes the characteristic diffusion length of VPI precursors and results in thorough metal oxide infiltration (vide infra).

PIM-1 Thin-Film Composite Membrane Fabrication. Matrimid 5218 support membranes were fabricated via nonsolvent-induced phase inversion. Matrimid 5218, tetrahydrofuran, ethanol, water, $LiNO_3$, and *N*-methyl-2-pyrrolidone were mixed with a mass ratio of 16:10:3:1:1:69 in a sealed container. Once the polymer was fully dissolved, the homogeneous solution was then cast into a liquid film via a blade on a clean glass plate. The liquid film was then transferred to a well-ventilated hood to assist the formation of a partial skin layer. After 30 s, the liquid film was immersed in a deionized water bath. Phase inversion was completed within 1 h resulting in an opaque porous membrane. The membrane was then stored in a new water bath for 12 h, followed by three washing cycles in methanol and three washing cycles in *n*-hexane sequentially. During each washing step, the membrane was immersed in the solvent bath for 3 h. After vacuum drying at 200 °C for 12 h, these support membranes were stored in the ambient environment before cross-linking. These Matrimid membranes were cross-linked by *p*-xylylenediamine. Dry Matrimid membranes were immersed in 10 wt % *p*-xylylenediamine methanol solution for 24 h at room temperature. After cross-linking, the membranes were washed with methanol and *n*-hexane three times. After vacuum drying at 100 °C for 12 h, these cross-linked Matrimid support membranes were stored in a sealed vessel that was saturated with hexane vapor. PIM-1 thin films were coated onto these cross-linked Matrimid support membranes via spin coating. A 0.5 wt % PIM-1 in chloroform solution at 4 °C was dropped onto the cross-linked Matrimid support membranes and spun at 500 rpm for 1 min and then ramped to 1000 rpm for 10 min. Before and during the spin-

DOI: 10.1021/acs.chemmater.9b01141
Chem. Mater. 2019, 31, 5509−5518

coating process, the membrane-processing chamber was saturated with chloroform vapor to slow the drying process. After spin coating, the resulting PIM-1 thin-film composite membranes were dried under vacuum at 100 °C for 24 h.

Vapor Phase Infiltration. Vapor phase infiltration was carried out in a custom-built 1 ft^3 (0.028 m^3) cubic hot-wall reactor (Figure S1). Prior to infiltration, PIM-1 materials (with the exception of the thin-film composites) were soaked in methanol for 2 h and dried in a fume hood for 30 min. The chamber was operated at 90 °C and prior to infiltration was purged with a 250 sccm ultrahigh purity nitrogen (Airgas, 99.999%) for between 5 and 15 h (depending upon the mass of PIM-1 in the chamber) to remove excess methanol and water. Following purging, the chamber was pumped down to baseline (~60 mTorr). Into the evacuated chamber, metal-organic precursors from Strem Chemicals (trimethylaluminum [98%, DANGER: pyrophoric], diethylzinc [95%, DANGER: pyrophoric], or titanium tetrachloride [97% DANGER: can generate corrosive HCl byproducts]) were dosed from room temperature into the chamber for 1 s unless otherwise noted (chamber pressure reached ~300 mTorr). The PIM-1 material within the chamber was exposed to the static precursor environment for various times (5 h in this work, unless otherwise noted). After the prescribed time, the chamber was purged with nitrogen for 5 min and evacuated to baseline in a 5 min pumpdown. Room-temperature deionized water vapor was then dosed for 5 s (~1.5 Torr) and exposed to the PIM-1 material for a time equivalent to precursor exposure. The chamber was purged and evacuated again for 5 min each before repeating the cycle (two total cycles were used unless otherwise noted). Following each purge and evacuation, a 2 min isolation step occurred that was used to validate the removal of most byproducts (Figure S1d). Materials were removed promptly once the process was completed. VPI recipes were automated via custom Labview control software.[46]

Fourier-Transform Infrared Spectroscopy. Fourier-transform infrared (FTIR) spectroscopy was used to characterize changes in the vibrational spectrum of PIM-1's functional groups after VPI. Flat PIM-1 films (10 μm) were thoroughly infiltrated with AlO_x, ZnO_x, and TiO_x (90 °C, two cycles of VPI, 5 h exposures) and characterized with a Thermo Scientific iS50 FTIR spectrometer (Thermo Fisher Scientific) using transmission mode.

X-ray Photoelectron Spectroscopy (XPS). X-ray photoelectron spectroscopy (XPS) was used to determine the existence and chemical-bonding states of hybrid materials. PIM-1 hollow fiber membranes thoroughly infiltrated with AlO_x, ZnO_x, and TiO_x (90 °C, two cycles of VPI, 5 h exposures) were ground into fine powders and analyzed with a Thermo K-alpha XPS (Thermo Fisher Scientific). Since metal oxide/PIM-1 hybrids are nonconductive, electrons aggregated on the sample surface resulting in significant peak shifts. Peak position was calibrated via an internal standard method. For each hybrid material, two pools of sample powders were prepared, one of which was mixed with silver nanoparticles. C 1s peak position was first calibrated according to the Ag 3d peaks detected in the sample mixed with silver nanoparticles. The other peaks in the sample without additives were then calibrated according to the C 1s peak shifts. Metal oxides were also coated onto silicon wafers via atomic layer deposition and analyzed by XPS. O 1s peak positions of these metal oxides were used as a comparison.

Solid-State NMR. Solid-state NMR was used to identify chemical states of carbon, hydrogen, and aluminum atoms in the hybrid materials. PIM-1 hollow fiber membranes thoroughly infiltrated with AlO_x, ZnO_x, and TiO_x (90 °C, two cycles of VPI, 5 h exposures) were ground into fine powders and packed into the zirconium NMR rotor. Solid-state NMR was then carried out via a Bruker Avance III 400.

X-ray Powder Diffraction (XRD). X-ray powder diffraction was used to analyze the crystallinity of the intertwined networks of metal oxide and PIM-1. PIM-1 hollow fiber membranes thoroughly infiltrated with AlO_x, ZnO_x, and TiO_x (90 °C, two cycles of VPI, 5 h exposures) were ground into fine powders and then analyzed by a Panalytical XPert PRO Alpha-1 XRD (Malvern Panalytical).

Transmission Electron Microscopy (TEM). Transmission electron microscopy (TEM) was used to determine the homogeneity of the hybrid material. TEM grids with carbon lace were dip-coated in a 0.5 wt % PIM-1 chloroform solution and dried in a glovebag filled with nitrogen. After a 24 h slow evaporation, the PIM-1-coated grids were further dried in vacuum at 100 °C for 24 h. The PIM-1-coated grids were then thoroughly infiltrated with AlO_x, ZnO_x, and TiO_x (90 °C, two cycles of VPI, 5 h exposures). The microstructure of the hybrid membranes on these grids was then analyzed with a Hitachi HT7700 TEM.

Scanning Electron Microscopy (SEM) and Energy-Dispersive X-ray (EDX) Spectroscopy. Cross-sectional images of the membranes were obtained with a Hitachi 8230 field emission scanning electron microscopy. Membranes were soaked in *n*-hexane for 10 min and fractured in liquid nitrogen to get clean cross sections. Crystallized hexane prevents the collapse of macropores during fracturing, and the low surface tension of hexane avoids the collapse of macropores and mesopores during evaporation. Fractured membranes were also sputtered with gold to reduce electron charging. Energy-dispersive X-ray (EDX) spectroscopy was used to obtain the element mapping of the membranes.

Thermogravimetric Analysis (TGA). Weight loading of metal oxides in PIM-1 membranes was determined by thermogravimetric analysis (TGA Q500, TA Instruments). Hollow fiber membranes were placed in platinum sample pans and heated in flowing air. During each thermogravimetric analysis run, the temperature was first maintained at 110 °C for 1 h to get rid of trapped moisture. After this in situ drying process, the temperature was ramped to 900 °C at 10 °C/min. The remaining mass was assumed to be the inorganic loading fraction, and the weight percent was calculated as the mass remaining after burnout over the mass of the fiber following the drying step. PIM-1 hollow fiber membranes treated with methanol and infiltrated with AlO_x (two-cycle VPI at 90 °C with 5 h exposures) were transformed into porous alumina hollow fibers (Figure S7) as byproducts of thermogravimetric analysis.

UV−Vis Spectroscopy for Dissolution. An Avantes Avaspec-2048 UV−vis spectrometer with a halogen light source was used to determine dissolution percentages of PIM-1 and AlO_x/PIM-1 in tetrahydrofuran with time. Short-term experiments (up to several hours) were conducted, where a treated or untreated hollow fiber membrane with known mass was placed directly in a cuvette with a known amount of tetrahydrofuran. Measurements were automatically collected with the software over time. Absorption values were translated into concentrations using Beer's law and a set of reference standards. Reference standards were prepared by dissolving a known amount of PIM-1 in a known amount of tetrahydrofuran (THF), performing serial dilutions, and collecting spectra. Long-term measurements (over a few hours) were conducted in vials containing a known mass of hollow fiber membrane and a known volume of THF. Aliquots were taken from these vials and diluted prior to measurement with UV−vis to ensure absorption values in the range of Beer's law. For AlO_x/PIM-1 membranes, the mass contribution of PIM-1 was determined based on percent AlO_x by weight from the TGA results. This adjusted mass contribution was used to determine the fully dissolved concentration of PIM-1 in the cuvette or vial. The fully dissolved concentration served as the denominator for determining percent dissolution, with the results from Beer's law being in the numerator.

Nitrogen Physisorption. Nitrogen physisorption was conducted at 77 K using a BELSORP-max (MicrotracBEL). PIM-1 hollow fiber membranes infiltrated with metal oxides were ground into fine powders and then dried under vacuum at 110 °C for 12 h. Brunauer−Emmett−Teller (BET) surface areas were calculated from the low-pressure region ($p/p^{sat} < 0.3$) of the cryogenic nitrogen physisorption isotherm. Pore size distribution was calculated via a N_2 DFT model.

Mercury Porosimetry. Mercury porosimetry was conducted by an AutoPore IV (Micromeritics) porosimeter. Prior to the measurement, PIM-1 hollow fiber membranes were cleaned with *n*-hexane and then dried under vacuum at 110 °C for 12 h.

Toluene and Water Uptake. Toluene and water isotherms were measured using a dynamic vapor sorption system (DVS Vacuum, Surface Measurement Systems). PIM-1 hollow fiber membranes with

DOI: 10.1021/acs.chemmater.9b01141
Chem. Mater. 2019, 31, 5509−5518

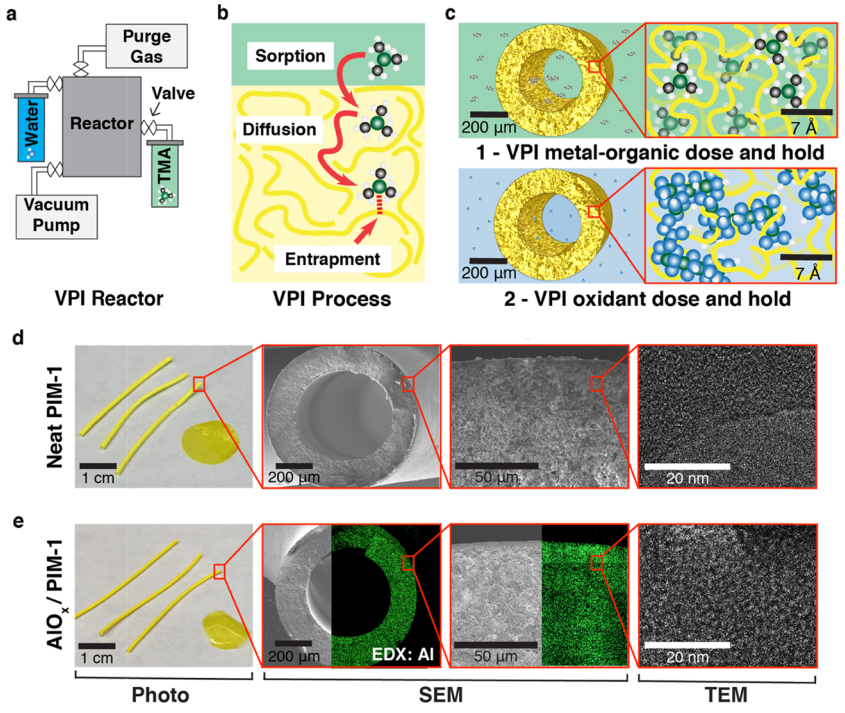

Figure 1. Schematic of vapor phase infiltration (VPI) and morphology characterization of pristine and hybrid PIM-1 membranes. (a) Diagram of the reactor used for VPI. Precursors are dosed into a static vapor environment. The chamber is pumped and purged with nitrogen between the precursor and coreactant doses. (b) Schematic depiction of VPI process: precursor sorption, diffusion, and entrapment (coordination or chemical reaction). (c) Schematic depiction of (1) metal-organic precursors sorbing into the PIM-1 microporosity and becoming trapped and (2) water vapor sorbing into the structure and reacting with the metal-organic to form an intertwined metal oxide network. In this report, the infiltration of precursors and coreactants is often cycled twice to increase the inorganic loading. (d, e) Photographs, SEM images, and TEM images of (d) PIM-1 before infiltration and (e) PIM-1 after infiltration with trimethylaluminum and water (two cycles). Green pixels in EDX map show aluminum distribution throughout the hybrid membrane.

and without VPI treatment were placed and in-situ-dried at 110 °C in the sample chamber of the DVS. The samples were then exposed to toluene or water vapors of a prescribed pressure at 25 °C. Equilibrium criteria were set to less than 0.001 wt % change within 10 min. Each isotherm was determined at least three times to calculate a standard deviation.

Contact Angle. Water contact angle measurements were conducted on a Ramé-Hart model 250 goniometer/tensiometer using drop size volumes of 10 μL. Measurements and photographs of untreated and VPI-treated PIM-1 flat membranes were taken 5 min after dispensing.

Organic Solvent Nanofiltration (OSN) and Organic Solvent Reverse Osmosis (OSRO). OSN and OSRO experiments were conducted in a customized cross-flow permeation system (Figure S10). During the OSN experiments, styrene dimer, polystyrene oligomers, 1,3,5-triisopropylbenzene, and 1,3-diisopropylbenzene were used as marker solutes to measure the molecular-weight cutoff of the membranes in ethanol, *n*-heptane, tetrahydrofuran, and toluene. During the OSRO experiments, alchohol mixtures (methanol, ethanol, and propanol) and aromatic mixtures (toluene, 1,3-diisopropylbenzene, and 1,3,5-triisopropylbenzene) were used to quantify the molecule differentiation capability of the membranes. Feed solutions were pressurized and delivered by an Azura P 4.1S pump (KNAUER). Feed flow rate was set to at least 10 times that of the permeation rate. Transmembrane pressure was maintained at 10 bar for thin-film composite membranes and 10 psi for hollow fiber membranes (pristine PIM-1 hollow fiber membranes cannot withstand higher pressures than this when exposed to ethanol). Permeates were collected in glass sample vials. The Thermo Evolution 220 UV–vis system (Thermo Fisher Scientific) was used to determine the dye rejection, an Agilent 1260 high-performance liquid chromatography was used to determine the change of marker solute concentration after OSN experiments, and an Agilent gas 7890 chromatography was used to determine the change of organic solvent composition after OSRO.

RESULTS AND DISCUSSION

Microstructure of the Metal Oxide/PIM-1 Hybrid Membranes. Vapor phase infiltration of PIM-1 hollow fiber membranes with several different metal-organic precursors results in amorphous metal oxide homogeneously distributed throughout the polymer bulk. Figure 1a–c illustrates how the VPI process creates metal oxide/PIM-1 hybrid membranes. Pristine PIM-1 membranes (e.g., thin-film composites, hollow fiber membranes, or freestanding membranes) are fabricated and then placed in a customized isothermal reaction chamber maintained at 90 °C (Figure 1a). After evacuation to rough vacuum (60 mTorr), the membranes are sequentially exposed to metal-organic precursors (trimethylaluminum [TMA], diethylzinc [DEZ], or titanium tetrachloride [$TiCl_4$]) and water vapor. During metal-organic precursor exposure, precursor molecules sorb and diffuse into the PIM-1 membranes (Figure 1b).

After a purge–pump cycle to remove byproducts (Figure S1d), the membrane, which is now saturated with metal-organic precursors, is exposed to water vapor. The metal-organic and water react within the membrane, creating an intertwined metal oxide network (Figure 1c). By varying the exposure times and the number of cycles, the amount and depth of inorganic infiltration can be engineered (Figure S2). Figure 1d,e presents photographic and electron microscopy analyses of the microstructure and chemical composition of pristine PIM-1 membranes and PIM-1 membranes infiltrated

DOI: 10.1021/acs.chemmater.9b01141
Chem. Mater. 2019, 31, 5509–5518

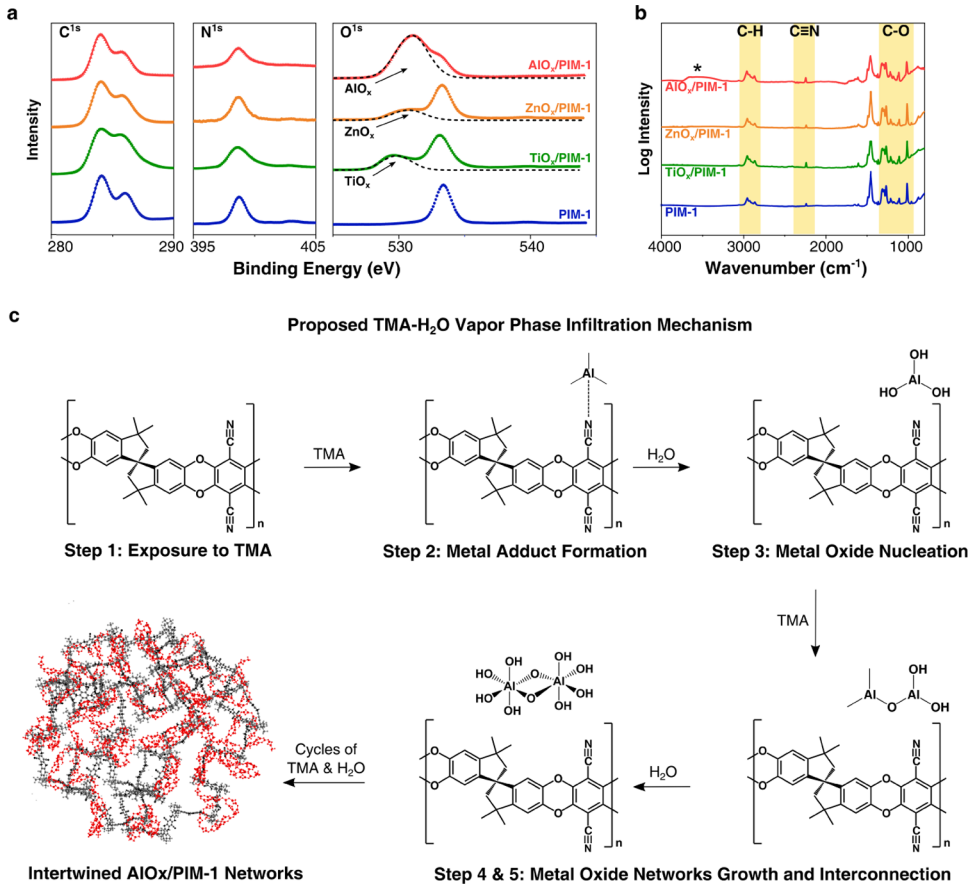

Figure 2. Chemical characterization of pristine PIM-1 and metal oxide/PIM-1 hybrids. (a) C 1s, N 1s, and O 1s XPS spectra and (b) logarithmic FTIR spectra for pristine PIM-1 and PIM-1 infiltrated with AlO_x, ZnO_x, and TiO_x. *Broad hydroxyl peaks are induced by absorbed water. (c) Proposed mechanism for metal oxide network formation via TMA VPI of PIM-1. The figures of the metal oxide network are provided only for illustration.

with aluminum oxide networks (AlO_x/PIM-1). The infiltrated, hybrid membranes show a negligible change in macrostructure (Figure 1e), and, at the microscale, the inorganic constituent is fairly homogeneously dispersed throughout the entire polymer (SEM/EDX). It is noted that there is a concentration of aluminum signal in the top portion of the hollow fiber membranes. This concentration is indicative of the denser polymer layer at the surface of the fiber that functions as the true separation membrane. Owing to the microporosity of PIM-1, there is no formation of impermeable metal oxide barrier layers on the surface of the membrane. As shown in Figure S2, metal oxides have been found to infiltrate 35 μm into a dense PIM-1 film with a classical diffusion-controlled distribution of metal oxide below the surface. The formation of infiltrated metal oxide within microporous polymers differentiates VPI from ALD. In ALD, impermeable inorganic coatings are deposited on the surface of substrate material.

Even at the nano- to atomic scale, the inorganic constituent appears to be homogeneously distributed: no metal oxide nanoparticles are observed in TEM (Figure 1e), and no metal oxide crystallinity is detected with XRD (Figure S3). These results reveal that PIM-1 membranes accommodate homogeneous inorganic loading fractions up to 30 wt % without large changes in microstructure (Figure S4a).

Chemical Structure of the Metal Oxide/PIM-1 Hybrid Membranes. Extensive chemical characterization of these hybrid membranes has revealed homogeneous loading of the inorganic constituent with a negligible change to the polymer chemistry, suggesting unbound, intertwined polymer chains and metal oxide networks. Ex situ chemical characterization (Figure 2) indicates that the PIM-1 backbone remains unchanged after infiltration with various metal oxides. XPS results (Figure 2a) show a negligible change in the binding energy of PIM-1's nitrogen and oxygen, the atoms most likely to react with the metal-organic precursors. The formation of unbound metal oxides is apparent in the O 1s spectra (Figure 2a, 530.9, 530.5, and 529.7 eV for AlO_x, ZnO_x, and TiO_x, respectively) and the corresponding metal 2p electron spectra (Figure S5). These results are mirrored in solid-state ^{13}C NMR, solid-state ^{1}H NMR (Figure S6), and FTIR (Figure 2b), in that no shifts in peak locations or intensities occur for the polymer's structure. In total, these results imply that metal oxide clusters percolate throughout the hybrid structure but do not chemically bond to the PIM-1 polymer. We hypothesize that during VPI, metal-organic precursors form semipermanent adducts with PIM-1's nitrile groups, similar to the interaction previously observed between TMA and amine or nitro functional groups in other VPI-related processes.[42] Upon water exposure, these metal-organic precursors are oxidized, the adducts release, and the newly formed metal oxide clusters become unbound from the polymer (Figure 2c). Further condensation reactions and repeated VPI cycling can interconnect these metal oxide clusters into an inorganic network. Experiments with long-duration purging (25 h)

DOI: 10.1021/acs.chemmater.9b01141
Chem. Mater. 2019, 31, 5509−5518

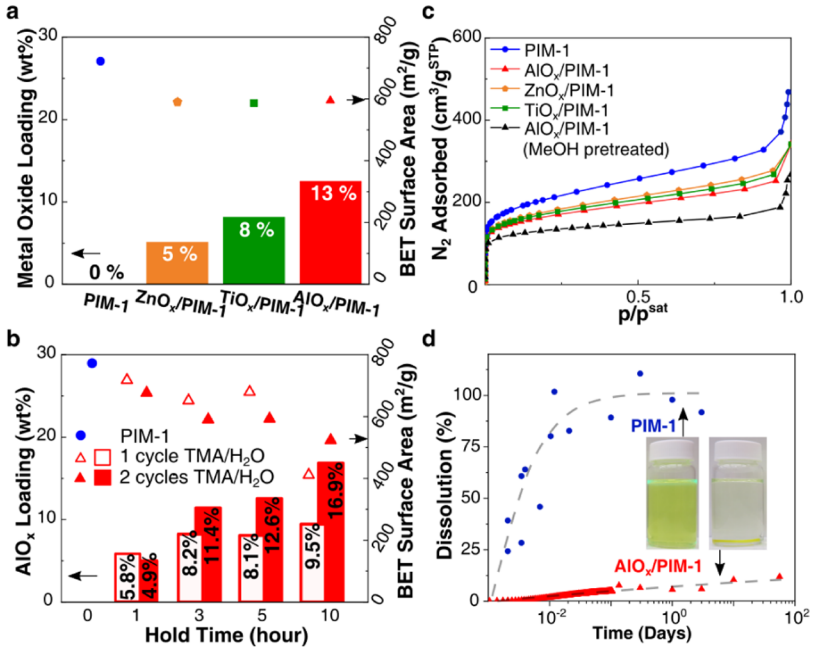

Figure 3. Influence of VPI chemistry and processing conditions on inorganic loading fraction, microporosity, and chemical stability of hybrid membranes. (a) metal oxide loading (bar graphs) and BET surface area (dot plots, errors are smaller than markers) of metal oxide/PIM-1 hybrids as a function of metal-organic chemistry. (b) metal oxide loading (bar graphs) and BET surface area (dot plots, errors are smaller than markers) of AlO_x/PIM-1 hybrid membranes as a function infiltration time and number of infiltration cycles. (c) Nitrogen isotherms at 77 K for pristine and infiltrated PIM-1 membranes (full adsorption−desorption isotherms are plotted in Figure S8a). (d) Dissolution of PIM-1 and AlO_x/PIM-1 membranes in THF determined via UV−vis. Dashed lines are included to guide the eye.

between precursor exposure and water dose (Figure S4b) further support this proposed mechanism. Regardless of purge time between the TMA and H_2O dosing, AlO_x/PIM-1 hybrids are found to have nearly equivalent inorganic mass loadings, supporting the formation of these semipermanent precursor−polymer adducts. Combusting the PIM-1 in air at high temperatures reveals the metal oxide network within these hybrid membranes. The resulting network is robust enough to image with SEM/EDX and investigate with cryogenic N_2 physisorption (Figure S7). From these techniques, the freestanding network still exhibited microporosity, supporting the existence of an inorganic network intertwined with PIM-1 chains, as well as supporting the presence of inorganic throughout the bulk of the PIM-1 hollow fiber membranes.

Effects of VPI-Processing Conditions on metal oxide Loading, Microporosity, and Chemical Stability in Organic Solvents. VPI-processing conditions can control the metal oxide loading fraction in the hybrid membrane. Optimal hybrid membrane performance requires balancing the trade-off between chemical stability (vide infra) and decrease in microporosity that comes with metal oxide loading. To investigate the influence of metal oxide loading fraction on microporosity, precursor exposure time and the number of infiltration cycles were adjusted to give different loading fractions. PIM-1 hollow fiber membranes with a moderate skin layer thickness (compared to thick-skinned flat dense membranes) and hierarchical porosity were utilized to enhance the diffusion kinetics (Figures S4c and S8). Here, the amount of metal oxide loading is quantified with thermogravimetric analysis (TGA), and the microporosity of the hybrid membranes is measured via N_2 physisorption. Results are presented in Figure 3 and are collected from PIM-1 hollow fiber membranes infiltrated with three different metal-organic precursors: TMA, DEZ, and $TiCl_4$. These data show that VPI chemistry and processing conditions affect the amount of metal oxide loading. The AlO_x/PIM-1 hybrid membrane shows significantly higher metal oxide loading than the other chemistries, yet exhibits nearly identical internal surface area, with only an 18% drop in surface area compared to pristine PIM-1 (Figure 3a). Generally, longer VPI exposure times or more VPI cycles increase metal oxide loading, deepen metal oxide penetration, and decrease BET surface area (Figures 3b,c and S2). Pretreatment of PIM-1 with methanol, which is known to reverse PIM-1's aging and temporarily increase free volume,[45,47] also increases metal oxide loading (Figure S4a). It is worth noting that vapor phase infiltration is a kinetically complex process involving sorption, diffusion, and reactions (Figure S2). Since diffusion is a significant component of this process, the infiltration time required to achieve full saturation of a polymer with metal oxides is approximately proportional to the square of the characteristic length of diffusion (e.g., half the thickness of the membrane skin layer).[19] Considering the relatively high skin layer thickness (~5 μm) of the hollow fiber membranes, the infiltration time can be significantly reduced by moving to membranes with thinner skin layers, such as thin-film composite membranes (skin layer thickness of ~150 nm). Therefore, the amount of metal oxide loading within a PIM-1 membrane can be controlled by the membrane's skin layer thickness, the precursor exposure time, pretreatment processing, precursor chemistry, VPI process temperature, and the number of VPI cycles.

Once transformed, these hybrid membranes show dramatic improvements in chemical stability. When tested against good solvents for PIM-1 (tetrahydrofuran (THF), dichloromethane (DCM), and chloroform ($CHCl_3$), all of which dissolve PIM-1 within minutes), all hybrid membranes show improved stability, many remaining stable throughout 3 months of testing (Movie S1). Among the hybrid membranes studied

DOI: 10.1021/acs.chemmater.9b01141
Chem. Mater. 2019, 31, 5509−5518

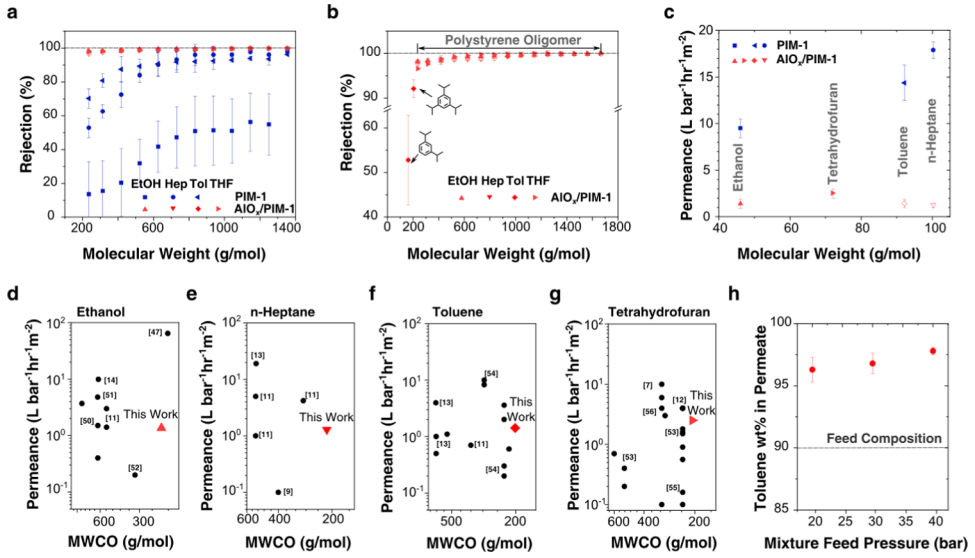

Figure 4. Organic solvent nanofiltration (OSN) and organic solvent reverse osmosis (OSRO) performances of PIM-1 and AlO$_x$/PIM-1 hybrid thin-film composite membranes (two cycles of TMA and H_2O infiltration, with 10 min precursor exposures). (a) Molecular-weight cutoff curves of PIM-1 and AlO$_x$/PIM-1 thin-film composites in different solvents using polystyrene oligomers as markers. (b) Detailed molecular-weight cutoff curves of AlO$_x$/PIM-1 thin-film composites using polystyrene oligomers, 1,3,5-triisopropylbenzene, and 1,3-diisopropylbenzene as markers. (c) Steady-state organic solvent permeance of PIM-1 and AlO$_x$/PIM-1 thin composite films under a 30 bar transmembrane pressure. OSN performance comparison with the literature in (d) ethanol,[11,14,49−52] (e) *n*-heptane,[11,51] (f) toluene,[11,53] and (g) tetrahydrofuran.[7,13,14,53−56] (h) Organic solvent reverse osmosis separation of toluene (90 wt %) from 1,3,5-triisopropylbenzene (5 wt %) and 1,3-diisopropylbenzene (5 wt %).

here, AlO$_x$/PIM-1 membranes exhibited the highest solvent stability. The low stability of the ZnO$_x$ and TiO$_x$ chemistries may be due to their lower levels of loading, which could prevent metal oxide network formation and provide insufficient entanglement with PIM-1 chains. Figure 3d illustrates the long-term stability of AlO$_x$/PIM-1 membranes in THF. While PIM-1 membranes fully dissolve within minutes, AlO$_x$/PIM-1 hybrid membranes lose only 10% of their weight after 1 month of immersion. These results suggest that the intertwined metal oxide network inhibits polymer reptation and retards dissolution. These hybrid membranes exhibit negligible swelling in toluene vapors (Figure S9a) and more Langmuir-type N_2 isotherms with increasing metal oxide loading (Figures 3c and S8). The hybrid membranes also show a change in hydrophilicity, as proven by both water sorption experiments and water contact angle measurements that could open new pathways for aqueous separations (Figure S9b,c).

AlO$_x$/PIM-1 Membranes for Organic Solvent Separation. To evaluate the organic solvent nanofiltration (OSN) and organic solvent reverse osmosis (OSRO) performances of these hybrid membranes, AlO$_x$/PIM-1 thin-film composite membranes were tested in a continuous cross-flow filtration system (Figure S10a) with ethanol, *n*-heptane, toluene, and tetrahydrofuran as solvents. PIM-1 thin-film composites were fabricated on cross-linked Matrimid 5218 supports via spin coating and then underwent two VPI cycles of TMA−H_2O with 10 min precursor exposure times at 90 °C.

Figure 4a plots the polystyrene oligomer retention of these membranes as a function of molecular weight in ethanol, *n*-heptane, toluene, and tetrahydrofuran. This plot illustrates the size-based molecular separation performance of the membranes in different solvent environments. For the thin, pristine PIM-1 membranes, the 90% molecular-weight cutoff (MWCO; the smallest molecular weight the membrane "successfully" rejects) is about 600 g/mol in *n*-heptane and toluene, solvents that do not significantly swell or plasticize PIM-1. However, in ethanol, a solvent that is known to plasticize and significantly swell PIM-1, the pristine polymer membranes fail to reject polystyrene oligomers less than 1200 g/mol. In tetrahydrofuran, the PIM-1 selective layer dissolves completely and no separation is possible. This loss of size-based separation performance in plasticizing solvents and dissolution in good solvents is consistent with prior separation experiments on pure, polymeric PIM-1 membranes reported in the literature.[13]

In contrast, hybrid AlO$_x$/PIM-1 membranes show consistent (more than 95%) polystyrene dimer rejection in all four solvents (ethanol, *n*-heptane, toluene, and tetrahydrofuran). Using 1,3,5-triisopropylbenzene and 1,3-diisopropylbenzene as marker "solutes", the MWCO of AlO$_x$/PIM-1 was determined to be 204 g/mol, which is 400 g/mol lower than the MWCO of the control PIM-1, and 100−200 g/mol lower than the MWCO for PIM-1 chemically cross-linked with poly(ethyleneimine).[11] The different rejection rates of these marker solutes exemplify the size-based molecular-sieving capabilities of the AlO$_x$/PIM-1 hybrid membrane (Figure S11). Diisopropylbenzene, with a critical diameter (5.5 Å) smaller than that of the AlO$_x$/PIM-1 hybrid's micropores (~6 Å, probed by nitrogen), permeates with less restriction (rejection = 52.8%) than triisopropylbenzene and styrene dimers that have critical diameters (6.7 Å) larger than the hybrid's micropores, which are mostly rejected (rejection >90%) by these membranes. This reduction in MWCO is expected based on the slight reduction of the membrane's micropore size from the infiltrated AlO$_x$ (Figures S8b and S9a). This smaller microporosity and narrower pore size distribution serve to improve the selectivity of these hybrid membranes in separations where precise molecular sieving between molecules with small-size differentials is needed (vide infra).

While the infiltration of AlO$_x$ decreases the membrane permeance by roughly 1 order of magnitude (Figure 4c), the AlO$_x$/PIM-1 thin composite membranes still deliver perme-

DOI: 10.1021/acs.chemmater.9b01141
Chem. Mater. 2019, 31, 5509−5518

ance comparable with state-of-the-art OSN membranes that exhibit MWCOs lower than 500 Da. Emerging membrane separation challenges require membranes with high selectivity, provided adequate permeances can be met.[1,4,48] As shown in Figure 4d−g, compared with other highly permeable membranes, the AlO_x/PIM-1 thin composite membrane provides unprecedented selectivity, which is indicated by the low MWCO (<204 Da). Moreover, after 1 week of OSN operation in each solvent, AlO_x/PIM-1 membranes did not exhibit any significant loss in inorganic component loading (Figure S12).

Also contributing to the improved performance of AlO_x/PIM-1 hybrid membranes for organic solvent separation is the modification of the hybrid membrane's mechanical properties (Figure S13a). The hybrid, freestanding hollow fiber membranes are found to be stiffer than the pristine polymer, as indicated by a greater Young's modulus. The hybrid membranes also show a modest decrease in their strength at break, as well as in their elongation at break. These results are expected as the inclusion of a ceramic material should result in a more brittle behavior relative to the pristine polymer. However, in dead-end OSN testing, the freestanding AlO_x/PIM-1 hollow fiber membranes withstand 1.6 times the pressure of pristine PIM-1 hollow fiber membranes in an equimolar mixture of THF and ethanol and twice the pressure in pure ethanol (Figure S13b,c). Therefore, while some mechanical properties are reduced relative to the pristine polymer, those that are most pertinent to separation performance show a marked improvement.

When performing OSN on dye molecules (Rose Bengal) in ethanol, AlO_x/PIM-1 hybrid hollow fiber membranes reject twice as much dye as pristine PIM-1 membranes (86 versus 43%, Figure S10b). This result suggests that the intertwined AlO_x networks within these hybrid membranes interrupt the strong interaction between these dye molecules and the membrane, reducing dye permeation through the membrane. VPI modification provides sufficient stabilization and resistance to swelling to enable the rejection of strongly sorptive solutes (such as Rose Bengal), which are typically challenging for polymer-based membranes to remove.[16]

Besides organic solvent nanofiltration, which separates solutes from solvents, AlO_x/PIM-1 membranes are also capable of organic solvent reverse osmosis (OSRO), which separates solvents from other solvents without a phase change.[3] A successful OSRO membrane must have relatively rigid, narrow micropores so that guest molecules exhibit distinctly different diffusivities.[8] Owing to guest-induced plasticization and swelling, common polymeric membranes usually cannot fulfill this requirement and therefore cannot differentiate between organic solvent molecules. Contrary to traditional polymeric membranes, AlO_x/PIM-1 membranes possess micropores with high resistance to swelling (Figure S8). As a result, AlO_x/PIM-1 hybrid membranes can potentially be used for certain OSRO operations. This capability was explored using a cross-flow system loaded with AlO_x/PIM-1 thin-film composite membranes, which were used to separate a mixture of a 90 wt % toluene, a 5 wt % 1,3,5-triisopropylbenzene, and a 5 wt % 1,3-diisopropylbenzene. By applying a transmembrane pressure of 40 bar (TMP, the hydraulic pressure difference across the membrane) beyond the osmotic pressure (eq S1) to the liquid mixture, the toluene concentration is enriched from 90.0 to 97.8 ± 0.3 wt % (Figure 4d). Moreover, AlO_x/PIM-1 thin-film composite membranes can be used to enrich the methanol concentration in methanol/ethanol mixtures from 99.0 to 99.8 ± 0.3 wt % (TMP = 30 bar, permeance = 8.1 ± 0.5 L m^{-2} h^{-1} bar^{-1}) and enrich the methanol concentration in the methanol/2-propanol mixtures from 90 to 95.4 ± 0.5 wt % (TMP = 30 bar, permeance = 7.8 ± 0.3 L m^{-2} h^{-1} bar^{-1}). The successful separation of these alcohol mixtures highlights the capability of AlO_x/PIM-1 membranes to differentiate molecules with small molecular-weight differences (∼14 Da). These preliminary results reveal the potential of AlO_x/PIM-1 membranes to enable challenging organic solvent separations and distillation debottlenecking via OSRO with minimally added energy.

CONCLUSIONS

In summary, vapor phase infiltration can be used to create unbound but intertwined atomic-scale metal oxide networks within nanoporous polymer membranes like PIM-1. Unlike pristine polymer membranes, these organic−inorganic hybrid membranes strongly resist swelling and dissolution in aggressive solvent environments. With this added chemical stability, hybrid PIM-1 membranes not only outperform untreated PIM-1 membranes for chemical separations in standard environments but also provide consistent performance in environments that would otherwise swell or even completely dissolve the pristine polymer. These membranes can even be applied for organic solvent reverse osmosis, which is difficult to realize using pristine PIM-1.

The unique, intertwined metal oxide/polymer structure proposed here, while likely generalizable, will certainly vary with polymer and precursor chemistries and VPI-processing conditions. Therefore, further exploration into the physiochemical structure and the processing conditions required to synthesize it is necessary. Ultimately, though, this work establishes a new, scalable, solvent-free, postsynthesis treatment for transforming nanoporous polymers into novel hybrid membranes with increased stability that have the potential to supplant energy-intensive distillation processes for organic solvent separations.

ASSOCIATED CONTENT

Supporting Information

The Supporting Information is available free of charge on the ACS Publications website at DOI: 10.1021/acs.chemmater.9b01141.

Vapor phase infiltration process; SEM/EDX scans of infiltration depth; XRD of pristine and infiltrated PIM-1; supplementary TGA data and long interim purge experimental results; supplementary XPS spectra; solid-state ^{1}H, ^{13}C, and ^{27}Al NMR; SEM of burned-out hollow fiber membrane and pore size analysis; cryogenic nitrogen physisorption and pore size distributions; water uptake and contact angle; OSN setup and results with various dyes; retention of inorganic component during organic solvent separation processes; mechanical stability of freestanding membranes; and calculation of osmotic pressure of toluene enrichment (PDF)

pristine and infiltrated PIM-1 membranes in THF, chloroform, and DCM (MP4)

AUTHOR INFORMATION

Corresponding Authors

*E-mail: ryan.lively@chbe.gatech.edu (R.P.L.).

DOI: 10.1021/acs.chemmater.9b01141
Chem. Mater. 2019, 31, 5509−5518

*E-mail: losego@gatech.edu (M.D.L.).

ORCID

Emily K. McGuinness: 0000-0003-4896-248X
Fengyi Zhang: 0000-0002-2398-8176
Yao Ma: 0000-0002-8283-8645
Ryan P. Lively: 0000-0002-8039-4008
Mark D. Losego: 0000-0002-9810-9834

Author Contributions

§E.K.M. and F.Z. contributed equally to this work.

Notes

The authors declare no competing financial interest.

■ ACKNOWLEDGMENTS

E.K.M. was supported by the Department of Defense (DoD) through the National Defense Science & Engineering Graduate Fellowship (NDSEG) Program. F.Z. and R.P.L. were supported by the National Science Foundation CAREER Award (CBET 1653153). Dr. Johannes Leisen assisted with the NMR measurements. The authors acknowledge the Specialty Separations Center at the Georgia Institute of Technology for equipment support. This work was performed, in part, at the Georgia Tech Institute for Electronics and Nanotechnology, a member of the National Nanotechnology Coordinated Infrastructure, which is supported by the National Science Foundation (Grant ECCS-1542174).

■ REFERENCES

(1) Sholl, D. S.; Lively, R. P. Seven chemical separations: to change the world: purifying mixtures without using heat would lower global energy use, emissions and pollution-and open up new routes to resources. *Nature* **2016**, *532*, 435−438.
(2) Koros, W. J.; Lively, R. P. Water and beyond: Expanding the spectrum of large-scale energy efficient separation processes. *AIChE J.* **2012**, *58*, 2624−2633.
(3) Koh, D.-Y.; McCool, B. A.; Deckman, H. W.; Lively, R. P. Reverse osmosis molecular differentiation of organic liquids using carbon molecular sieve membranes. *Science* **2016**, *353*, 804−807.
(4) Marchetti, P.; Jimenez Solomon, M. F.; Szekely, G.; Livingston, A. G. Molecular separation with organic solvent nanofiltration: a critical review. *Chem. Rev.* **2014**, *114*, 10735−10806.
(5) Lai, Z.; Bonilla, G.; Diaz, I.; Nery, J. G.; Sujaoti, K.; Amat, M. A.; Kokkoli, E.; Terasaki, O.; Thompson, R. W.; Tsapatsis, M. Microstructural optimization of a zeolite membrane for organic vapor separation. *Science* **2003**, *300*, 456−460.
(6) Kim, D.; Jeon, M. Y.; Stottrup, B. L.; Tsapatsis, M. para-Xylene Ultra-selective Zeolite MFI Membranes Fabricated from Nanosheet Monolayers at the Air−Water Interface. *Angew. Chem., Int. Ed.* **2018**, *57*, 480−485.
(7) Sorribas, S.; Gorgojo, P.; Téllez, C.; Coronas, J.; Livingston, A. G. High flux thin film nanocomposite membranes based on metal−organic frameworks for organic solvent nanofiltration. *J. Am. Chem. Soc.* **2013**, *135*, 15201−15208.
(8) Ma, Y.; Zhang, F.; Yang, S.; Lively, R. P. Evidence for entropic diffusion selection of xylene isomers in carbon molecular sieve membranes. *J. Membr. Sci.* **2018**, *564*, 404−414.
(9) Zhu, G.; Zhang, F.; Rivera, M. P.; Hu, X.; Zhang, G.; Jones, C. W.; Lively, R. P. Molecularly Mixed Composite Membranes for Advanced Separation Processes. *Angew. Chem.* **2019**, *131*, 2664−2669.
(10) Voigt, I.; Stahn, M.; Wöhner, S.; Junghans, A.; Rost, J.; Voigt, W. Integrated cleaning of coloured waste water by ceramic NF membranes. *Sep. Purif. Technol.* **2001**, *25*, 509−512.
(11) Fritsch, D.; Merten, P.; Heinrich, K.; Lazar, M.; Priske, M. High performance organic solvent nanofiltration membranes: Development and thorough testing of thin film composite membranes made of polymers of intrinsic microporosity (PIMs). *J. Membr. Sci.* **2012**, *401−402*, 222−231.
(12) Jimenez-Solomon, M. F.; Song, Q.; Jelfs, K. E.; Munoz-Ibanez, M.; Livingston, A. G. Polymer nanofilms with enhanced microporosity by interfacial polymerization. *Nat. Mater.* **2016**, *15*, 760.
(13) Cook, M.; Gaffney, P. R.; Peeva, L. G.; Livingston, A. G. Roll-to-roll dip coating of three different PIMs for Organic Solvent Nanofiltration. *J. Membr. Sci.* **2018**, *558*, 52−63.
(14) Liang, B.; Wang, H.; Shi, X.; Shen, B.; He, X.; Ghazi, Z. A.; Khan, N. A.; Sin, H.; Khattak, A. M.; Li, L.; Tang, Z. Microporous membranes comprising conjugated polymers with rigid backbones enable ultrafast organic-solvent nanofiltration. *Nat. Chem.* **2018**, *10*, 961.
(15) Zhang, F.; Ma, Y.; Liao, J.; Breedveld, V.; Lively, R. P. Solution-Based 3D Printing of Polymers of Intrinsic Microporosity. *Macromol. Rapid Commun.* **2018**, *39*, No. 1800274.
(16) Tsarkov, S.; Khotimskiy, V.; Budd, P. M.; Volkov, V.; Kukushkina, J.; Volkov, A. Solvent nanofiltration through high permeability glassy polymers: effect of polymer and solute nature. *J. Membr. Sci.* **2012**, *423−424*, 65−72.
(17) Budd, P. M.; Elabas, E. S.; Ghanem, B. S.; Makhseed, S.; McKeown, N. B.; Msayib, K. J.; Tattershall, C. E.; Wang, D. Solution-processed, organophilic membrane derived from a polymer of intrinsic microporosity. *Adv. Mater.* **2004**, *16*, 456−459.
(18) Koh, D.-Y.; Lively, R. P. Nanoporous graphene: Membranes at the limit. *Nat. Nanotechnol.* **2015**, *10*, 385−386.
(19) Leng, C. Z.; Losego, M. D. Vapor phase infiltration (VPI) for transforming polymers into organic−inorganic hybrid materials: a critical review of current progress and future challenges. *Mater. Horiz.* **2017**, *4*, 747−771.
(20) Azpitarte, I.; Knez, M. Vapor phase infiltration: from a bioinspired process to technologic application, a prospective review. *MRS Commun.* **2018**, *8*, 727−741.
(21) Subramanian, A.; Tiwale, N.; Nam, C.-Y. Review of Recent Advances in Applications of Vapor-Phase Material Infiltration Based on Atomic Layer Deposition. *JOM* **2019**, *71*, 185−196.
(22) Ingram, W. F.; Jur, J. S. Properties and Applications of Vapor Infiltration into Polymeric Substrates. *JOM* **2019**, *71*, 238−245.
(23) Yang, H. C.; Waldman, R. Z.; Chen, Z.; Darling, S. B. Atomic layer deposition for membrane interface engineering. *Nanoscale* **2018**, *10*, 20505−20513.
(24) Xu, Q.; Yang, Y.; Wang, X.; Wang, Z.; Jin, W.; Huang, J.; Wang, Y. Atomic layer deposition of alumina on porous polytetrafluoroethylene membranes for enhanced hydrophilicity and separation performances. *J. Membr. Sci.* **2012**, *415−416*, 435−443.
(25) Xu, Q.; Yang, Y.; Yang, J.; Wang, X.; Wang, Z.; Wang, Y. Plasma activation of porous polytetrafluoroethylene membranes for superior hydrophilicity and separation performances via atomic layer deposition of TiO2. *J. Membr. Sci.* **2013**, *443*, 62−68.
(26) Yang, H.-C.; Xie, Y.; Chan, H.; Narayanan, B.; Chen, L.; Waldman, R. Z.; Sankaranarayanan, S. K.; Elam, J. W.; Darling, S. B. Crude-Oil-Repellent Membranes by Atomic Layer Deposition: Oxide Interface Engineering. *ACS Nano* **2018**, *12*, 8678−8685.
(27) Nikkola, J.; Sievänen, J.; Raulio, M.; Wei, J.; Vuorinen, J.; Tang, C. Y. Surface modification of thin film composite polyamide membrane using atomic layer deposition method. *J. Membr. Sci.* **2014**, *450*, 174−180.
(28) Juholin, P.; Käariäinen, M.-L.; Riihimäki, M.; Sliz, R.; Aguirre, J. L.; Pirilä, M.; Fabritius, T.; Cameron, D.; Keiski, R. L. Comparison of ALD coated nanofiltration membranes to unmodified commercial membranes in mine wastewater treatment. *Sep. Purif. Technol.* **2018**, *192*, 69−77.
(29) Li, N.; Tian, Y.; Zhao, J.; Zhang, J.; Kong, L.; Zhang, J.; Zuo, W. Static adsorption of protein-polysaccharide hybrids on hydrophilic modified membranes based on atomic layer deposition: Anti-fouling performance and mechanism insight. *J. Membr. Sci.* **2018**, *548*, 470−480.
(30) Li, N.; Tian, Y.; Zhang, J.; Sun, Z.; Zhao, J.; Zhang, J.; Zuo, W. Precisely-controlled modification of PVDF membranes with 3D

DOI: 10.1021/acs.chemmater.9b01141
Chem. Mater. 2019, 31, 5509−5518

TiO_2/ZnO nanolayer: enhanced anti-fouling performance by changing hydrophilicity and photocatalysis under visible light irradiation. *J. Membr. Sci.* **2017**, *528*, 359−368.
(31) Lee, A.; Libera, J. A.; Waldman, R. Z.; Ahmed, A.; Avila, J. R.; Elam, J. W.; Darling, S. B. Conformal Nitrogen-Doped TiO_2 Photocatalytic Coatings for Sunlight-Activated Membranes. *Adv. Sustainable Syst.* **2017**, *1*, No. 1600041.
(32) Wang, Q.; Wang, X.; Wang, Z.; Huang, J.; Wang, Y. PVDF membranes with simultaneously enhanced permeability and selectivity by breaking the tradeoff effect via atomic layer deposition of TiO2. *J. Membr. Sci.* **2013**, *442*, 57−64.
(33) George, S. M. Atomic layer deposition: an overview. *Chem. Rev.* **2010**, *110*, 111−131.
(34) Parsons, G. N.; George, S. M.; Knez, M. Progress and future directions for atomic layer deposition and ALD-based chemistry. *MRS Bull.* **2011**, *36*, 865−871.
(35) Puurunen, R. L. Surface chemistry of atomic layer deposition: A case study for the trimethylaluminum/water process. *J. Appl. Phys.* **2005**, *97*, No. 121301.
(36) Leng, C. Z.; Losego, M. D. A physiochemical processing kinetics model for the vapor phase infiltration of polymers: measuring the energetics of precursor-polymer sorption, diffusion, and reaction. *Phys. Chem. Chem. Phys.* **2018**, *20*, 21506−21514.
(37) Caligiore, F. E.; Nazzari, D.; Cianci, E.; Sparnacci, K.; Laus, M.; Perego, M.; Seguini, G. Effect of the Density of Reactive Sites in P (S-*r*-MMA) Film during Al2O3 Growth by Sequential Infiltration Synthesis. *Adv. Mater. Interfaces* **2019**, No. 1900503.
(38) Parsons, G. N.; Elam, J. W.; George, S. M.; Haukka, S.; Jeon, H.; Kessels, W.; Leskelä, M.; Poodt, P.; Ritala, M.; Rossnagel, S. M. History of atomic layer deposition and its relationship with the American Vacuum Society. *J. Vac. Sci. Technol., A* **2013**, *31*, No. 050818.
(39) Dusoe, K. J.; Ye, X.; Kisslinger, K.; Stein, A.; Lee, S.-W.; Nam, C. Y. Ultrahigh Elastic Strain Energy Storage in Metal-Oxide-Infiltrated Patterned Hybrid Polymer Nanocomposites. *Nano Lett.* **2017**, *17*, 7416−7423.
(40) Lee, S.-M.; Pippel, E.; Gösele, U.; Dresbach, C.; Qin, Y.; Chandran, C. V.; Bräuniger, T.; Hause, G.; Knez, M. Greatly increased toughness of infiltrated spider silk. *Science* **2009**, *324*, 488−492.
(41) Azpitarte, I.; Zuzuarregui, A.; Ablat, H.; Ruiz-Rubio, L.; López-Ortega, A.; Elliott, S. D.; Knez, M. Suppressing the Thermal and Ultraviolet Sensitivity of Kevlar by Infiltration and Hybridization with ZnO. *Chem. Mater.* **2017**, *29*, 10068−10074.
(42) Yang, F.; Brede, J.; Ablat, H.; Abadia, M.; Zhang, L.; Rogero, C.; Elliott, S. D.; Knez, M. Reversible and Irreversible Reactions of Trimethylaluminum with Common Organic Functional Groups as a Model for Molecular Layer Deposition and Vapor Phase Infiltration. *Adv. Mater. Interfaces* **2017**, *4*, No. 1700237.
(43) Obuchovsky, S.; Frankenstein, H.; Vinokur, J.; Hailey, A. K.; Loo, Y.-L.; Frey, G. L. Mechanism of metal oxide deposition from atomic layer deposition inside nonreactive polymer matrices: effects of polymer crystallinity and temperature. *Chem. Mater.* **2016**, *28*, 2668−2676.
(44) Padbury, R. P.; Jur, J. S. Effect of polymer microstructure on the nucleation behavior of alumina via atomic layer deposition. *J. Phys. Chem. C* **2014**, *118*, 18805−18813.
(45) Jue, M. L.; McKay, C. S.; McCool, B. A.; Finn, M.; Lively, R. P. Effect of Nonsolvent Treatments on the Microstructure of PIM-1. *Macromolecules* **2015**, *48*, 5780−5790.
(46) Piercy, B. D.; Losego, M. D. Tree-based control software for multilevel sequencing in thin film deposition applications. *J. Vac. Sci. Technol., B: Nanotechnol. Microelectron.: Mater., Process., Meas., Phenom.* **2015**, *33*, No. 043201.
(47) Budd, P. M.; McKeown, N. B.; Ghanem, B. S.; Msayib, K. J.; Fritsch, D.; Starannikova, L.; Belov, N.; Sanfirova, O.; Yampolskii, Y.; Shantarovich, V. Gas permeation parameters and other physicochemical properties of a polymer of intrinsic microporosity: Polybenzodioxane PIM-1. *J. Membr. Sci.* **2008**, *325*, 851−860.
(48) Marchetti, P.; Peeva, L.; Livingston, A. The selectivity challenge in organic solvent nanofiltration: membrane and process solutions. *Annu. Rev. Chem. Biomol. Eng.* **2017**, *8*, 473−497.
(49) Karan, S.; Samitsu, S.; Peng, X.; Kurashima, K.; Ichinose, I. Ultrafast viscous permeation of organic solvents through diamond-like carbon nanosheets. *Science* **2012**, *335*, 444−447.
(50) Vanherck, K.; Hermans, S.; Verbiest, T.; Vankelecom, I. Using the photothermal effect to improve membrane separations via localized heating. *J. Mater. Chem.* **2011**, *21*, 6079−6087.
(51) Volkov, A. V.; Parashchuk, V. V.; Stamatialis, D. F.; Khotimsky, V. S.; Volkov, V. V.; Wessling, M. High permeable PTMSP/PAN composite membranes for solvent nanofiltration. *J. Membr. Sci.* **2009**, *333*, 88−93.
(52) Vanherck, K.; Verbiest, T.; Vankelecom, I. Comparison of two synthesis routes to obtain gold nanoparticles in polyimide. *J. Phys. Chem. C* **2012**, *116*, 115−125.
(53) Jimenez-Solomon, M. F.; Gorgojo, P.; Munoz-Ibanez, M.; Livingston, A. G. Beneath the surface: Influence of supports on thin film composite membranes by interfacial polymerization for organic solvent nanofiltration. *J. Membr. Sci.* **2013**, *448*, 102−113.
(54) See Toh, Y. H.; Lim, F. W.; Livingston, A. G. Polymeric membranes for nanofiltration in polar aprotic solvents. *J. Membr. Sci.* **2007**, *301*, 3−10.
(55) Sairam, M.; Loh, X.; Bhole, Y.; Sereewatthanawut, I.; Li, K.; Bismarck, A.; Steinke, J.; Livingston, A. Spiral-wound polyaniline membrane modules for organic solvent nanofiltration (OSN). *J. Membr. Sci.* **2010**, *349*, 123−129.
(56) Székely, G.; Bandarra, J.; Heggie, W.; Sellergren, B.; Ferreira, F. C. Organic solvent nanofiltration: a platform for removal of genotoxins from active pharmaceutical ingredients. *J. Membr. Sci.* **2011**, *381*, 21−33.

DOI: 10.1021/acs.chemmater.9b01141
Chem. Mater. 2019, 31, 5509−5518